

Downloaded from https://academic.oup.com/mnras/article/496/2/1035/5850385 by guest on 17 May 202

An [O III] search for extended emission around AGN with H I mapping: a distant cloud ionized by Mkn 1

Erin Darnell Knese, ^{1,2,3} William C. Keel [®], ^{1,3}★ Greg Knese, ⁴ Vardha N. Bennert, ⁵ Alexei Moiseev [®], ⁶ Aleksandra Grokhovskaya ⁶ and Sergei N. Dodonov ⁶

Accepted 2020 May 24. Received 2020 May 5; in original form 2019 May 28

ABSTRACT

Motivated by the discovery of large ionized clouds around AGN, and particularly the large fraction of those that are consistent with photoionized gaseous tidal debris, we searched for [O III] emission around Seyfert galaxies previously mapped in H I, many with extended gas features. Of 26 Seyfert galaxies, we find one spatially extended emission feature, a discrete cloud projected \approx 12 kpc SW from the centre of Mkn 1 and spanning a transverse extent of 8 kpc. Optical spectroscopy (Kast/Lick and SCORPIO/BTA) of this cloud confirms its association with the Mkn 1–NGC 451 galaxy pair, closely matching the kinematics of nearby H I structures, and reveals emission-line ratios requiring photoionization by the AGN at roughly the direct observed luminosity of the nucleus. For the entire sample, the full opening angle of the ionization cones (bicones) must be <20° if the AGNs are continuously bright for scales longer than the light-traveltimes to the H I structures. Since typical AGN ionization cones are observed to be much broader than this, our low detection fraction may add to evidence for the ubiquity of strong variations in AGN luminosity on scales 10^4 – 10^5 yr.

Key words: galaxies: active-galaxies: individual (Mkn 1)-galaxies: ISM-galaxies: Seyfert.

1 INTRODUCTION

A subset of active galactic nuclei (AGNs) has been known to be accompanied by extended emission-line regions (EELRs), since pioneering discoveries in the 1980s. As reviewed by, for example, Wilson (1996) and Stockton, Fu & Canalizo (2006), these often take the form of ionization cones, and in some cases extend tens of kpc outside the AGN host galaxy itself. EELRs allow us to trace the pattern of emerging radiation, characterize AGNs that are strongly obscured along our line of sight, or have undergone dramatic luminosity changes over millennia. These applications have seen new use with recent discoveries of EELRs around AGNs that appear too faint to account for their ionization level, requiring either strong obscuration or strong variability (over the light-traveltimes between nucleus and EELR) to explain this mismatch. In particular, Hanny's Voorwerp (Lintott et al. 2009; Schawinski et al. 2010; Keel et al.

2012b) is a galaxy scale¹ highly ionized cloud for which the nearby AGN in IC 2497 fails to be able to account for its ionization by factors of 20–100 even when its spectral energy distribution up to hard X-rays is modelled (Sartori et al. 2016). Following the discovery of this object by Galaxy Zoo participant Hanny van Arkel, a dedicated search by additional Galaxy Zoo participants found another 19 AGNs with similar ionized clouds projected > 10 kpc from the nuclei (Keel et al. 2012a), of which 8 have a substantial energy deficit from the AGN as observed (Keel et al. 2017b). Additional studies have identified analogous objects at both lower and higher AGN luminosity (Schirmer et al. 2013; Schweizer et al. 2013).

These findings have allowed the beginnings of a picture of AGN changes over time spans 10^4 – 10^5 yr, which can connect to longer time spans inferred from simulations and statistics of AGN in interacting hosts, and with the shorter time-scales known from direct observations (reverberation studies and the growing number of 'changing-look' AGN). If the AGN surrounded by

¹Department of Physics and Astronomy, University of Alabama, Box 870324, Tuscaloosa, AL 35487, USA

²Current address: Husch Blackwell, 190 Carondelet Plaza, Suite 600, St Louis, MO 63105, USA

³SARA Observatory, Embry-Riddle Aeronautical University, Melbourne, FL 32114, USA

⁴Department of Mathematics, Washington University in St Louis, One Brookings Drive, St Louis, MO 63130, USA

⁵Department of Physics, California Polytechnic State University, San Luis Obispo, CA 93407, USA

⁶Special Astrophysical Observatory, Russian Academy of Sciences, Nizhny Arkhyz 369167, Russia

^{*} E-mail: wkeel@ua.edu

¹The projected separation of the ionized cloud from the nucleus of its host galaxy IC 2497 spans 16–44 kpc.

EELRs are typical, their radiative output is characterized by luminous phases $\approx 10^5$ yr long with low-luminosity interludes, possibly associated with transitions between the accretion output being mostly radiative or mostly kinetic (Keel et al. 2012a, 2017b; Schawinski et al. 2015). The 'changing-look' AGNs (e.g. LaMassa et al. 2015; Runnoe et al. 2016; Ruan et al. 2016), which change their nuclear luminosity significantly within only a few years, show that such rapid changes in the AGN luminosity occur. In contrast, luminosity changes traced by ionized clouds tens of kpc from the AGN must represent millennium-scale periods when the average value remained high or low.

Since almost all EELRs have been found around galaxies with extant (sometimes low-luminosity) AGN, and surrounding gas is a prerequisite to their occurrence, we have carried out a series of imaging surveys in the strongest optical emission line from EELRs, [O III] $\lambda5007$, in search of distant nebulosities ionized by AGN, especially cases too faint to be detected in current broad-band sky-survey data. To this end, we select local (z<0.02) Seyfert galaxies mapped in H I (Kuo et al. 2008) for which we know which ones have extended H I discs or tails and for which we also know what fraction of each AGN host is surrounded by such gas.

We present here a detailed study of the Seyfert 2 galaxy, Mkn 1, the only object in the sample that shows extended emission line features interpretable as EELRs. Narrow-band imaging from the SARA-KP Observatory and optical spectroscopic (Kast/Lick and SCORPIO/BTA) data have been obtained. We report the evidence in this galaxy of a distant (\approx 12 kpc from the center of Mkn 1) and extended (\approx 8 kpc) cloud ionized by its AGN.

From studying the whole sample, we are able to obtain information on the covering factor of the escaping ionizing radiation (opening angle of ionization cones) combined with the fraction of the time the typical AGN is in a luminous state over the scales spanned by light-traveltimes to the outermost gas. An appendix presents a derivation of an analytical expression for the probability of intersection of a cone with randomly oriented arcs, approximating the geometry of H I clouds and tails exposed to ionization cones.

This paper is organized as follows. Section 2 describes the sample. Section 3 describes the observations and the data analysis. In the first part of Section 3.1, we describe the narrow-band imaging observations for the whole sample, while in the second part of Section 3.2 we present follow-up imaging and spectroscopic data used for the analysis of the sole object in which we found an EELR, Mkn 1. Section 4 is focused on the results obtained for Mkn 1 and its ionized cloud. In Section 5, we consider the implications of the entire sample for the ionization of EELR gas, in particular whether such a low detection fraction is consistent with the observed widths of ionization cones and long durations for AGN luminous phases, while the conclusions are presented in Section 6. Appendix A gives the derivation of an analytic expression for the probability of a bicone (i.e. a pair of ionization cones) to intercept randomly oriented arcs about an AGN, while in Appendix B, potential compact emission-line candidates in the field of view of the target galaxies are identified.

In quoting luminosities and sizes, we adopt $H_0 = 72 \text{ km s}^{-1}$ Mpc⁻¹ and flat cosmological geometry. At the redshifts of our sample, this gives a linear scale ranging from 0.30 to 0.39 kpc arcsec⁻¹.

2 SAMPLE

Our sample consists of the Seyfert galaxies observed by Kuo et al. (2008) in their study of H I structures around active galaxies,

including the objects for which the HI data were presented earlier by Greene, Lim & Ho (2004). We consider all the AGNs in the combined H I sample, omitting Mkn 1158 and Mkn 1510 since their nuclei are dominated by star formation rather than AGN. This leaves 26 Seyfert galaxies in our sample (Table 1). They lie at redshifts z =0.015–0.020; for guidance, we include Hubble types from Kuo et al. (2008) and AGN classifications from NED.2 Nuclear fluxes in the $[O III] \lambda 5007$ emission line are from spectrophotometry of the nuclei in the literature (apertures usually 2–6 arcsec, as listed in Table 1), or if no such data are available, from our continuum-corrected images, since colour variations can give systematic errors for nuclei when the difference images are best scaled for each galaxy's outskirts. Even spectrophotometric measurements can scatter by more than a factor of 2 for nominally nuclear values, likely due to the partly resolved structure of the narrow-line region (Whittle 1992), so these flux values from heterogeneous sources are best regarded as indicative.

This survey is the first phase of a multipart programme we call TELPERION.³ Further phases now in progress encompass merging galaxies in the Toomre sequence, luminosity-selected AGN, luminous galaxies independent of AGN, and a larger merging sample from the Galaxy Zoo (Lintott et al. 2008) analysis by Darg et al. (2010).

3 OBSERVATIONS AND DATA ANALYSIS

3.1 Observations: narrow-band imaging

The survey observations were carried out between 2010 October and 2012 July using the remotely operated telescopes of the SARA Observatory (Keel et al. 2017a). The narrow-band images, and most of the broad-band continuum imaging, used the 1m instrument on Kitt Peak, Arizona (SARA-KP). During this period, it was equipped with a 2048 pixel \times 2048 pixel E2V CCD in an Apogee U42 camera. The pixel scale was 0.382 arcsec pixel⁻¹, giving a field 13.04 arcmin². For a centred galaxy, this meant the images covered (inscribed) projected radii 118–153 kpc over the redshift range of our sample. The *V*-band continuum images for five galaxies (MS 04595+0327, UGC 1395, NGC 7591, NGC 7679, and NGC 7682) were obtained using the SARA 0.6m telescope on Cerro Tololo, Chile. The Apogee Alta E6 camera then in use gave a field 10.34 arcmin² at 0.606 arcsec pixel⁻¹, covering radial regions out to \approx 100 kpc from each targeted galaxy.

A narrow-band filter centred at 5100 Å with half-transmission points at 5047 and 5132 Å captured [O III] emission at the redshifts of sample members. The filter is circular with a 50 mm diameter, and was fabricated by Custom Scientific. Corners of the CCD images are slightly vignetted, an effect well corrected using twilight-sky flat fields. A standard V passband, which has its centre of transmission close to the narrow-band filter's peak transmission, was used for comparison images in the broad-band continuum.

In the converging f/8 beam of this telescope, we expect the peak response of the [O III] filter to be shifted bluewards by about 10 Å, which we correct in deriving emission-line fluxes. Our exposures were designed to reach mean emission-line surface brightness at least 10 times fainter than Hanny's Voorwerp, which has a mean

²The NASA Extragalactic Database, http://ned.ipac.caltech.edu.

³The name stands for Tracing Emission Lines to Probe Extended Regions Ionized by Once-active Nuclei, and is intended to connote long-vanished brilliance for readers of Tolkien's work on the First Age of Middle-Earth.

⁴http://customscientific.com

Table 1. Properties of sample galaxies.

Name	z	M_B	AGN type Class	Hubble type	Inclination $(^{\circ})$	$F_{\rm NUC}(5007)$ (erg cm ⁻² s ⁻¹)	Aperture (arcsec)	Flux reference
Mkn 341	0.0153	-21.9	S	S0-a	70.5	1.1×10^{-14}	4.7	Keel et al. (1985)
NGC 266	0.0155	-20.6	S3b	Sab	14.5	5.7×10^{-15}	2×4	Ho, Filippenko & Sargent (1997)
Mkn 352	0.0149	-19.5	S1.0	S0	33.9	2.5×10^{-14}	3.6×3.6	Mulchaey, Wilson & Tsvetanov (1996)
Mkn 1	0.0159	-19.0	S2	Sb	58.7	5.4×10^{-13}	6.0	Balick & Heckman (1979)
NGC 513	0.0195	-21.5	S1h	Sc	61.9	1.4×10^{-13}	30×35	Mulchaey et al. (1996)
Mkn 993	0.0155	-20.0	S1.5	Sa	90.0	4.8×10^{-13}	42×132	Robitaille et al. (2007)
Mkn 359	0.0174	-20.2	NLS1	Sb	39.1	1.1×10^{-13}	11×15	Mulchaey et al. (1996)
Mkn 1157	0.0152	-20.1	S1h	S0-a	40.2	2.1×10^{-13}	10×10	Mulchaey et al. (1996)
Mkn 573	0.0172	-20.1	S1h	S0-a	28.0	9.3×10^{-13}	2×4	de Grijp et al. (1992)
UGC 1395	0.0174	-20.5	S1.9	Sb	54.8	6.0×10^{-14}	2×4	Phillips, Charles & Baldwin (1983)
NGC 841	0.0151	-21.4	S3b	Sab	64.8	1.3×10^{-15}	2×4	Ho et al. (1997)
Mkn 1040	0.0167	-19.2	S1.0	Sbc	81.1	7.5×10^{-14}	1×3	de Grijp et al. (1992)
NGC 1167	0.0165	-21.1	S2	S0	49.0	2.9×10^{-14}	2×4	Ho et al. (1997)
UGC 3157	0.0154	-19.9	S2	Sbc	35.2	6.4×10^{-15}	10	This work
MS 04595+0327	0.0160	-19.5	S 1	S?	50.2	1.5×10^{-13}	2:	Ghigo et al. (1982)
IRAS	0.0179	-19.4	S1.5	E?	39.7	1.9×10^{-14}	2.5	Wang, Wei & He (2006)
05078+1626								
UGC 3995A	0.0158	-21.5	S2	Sb	67.6	3.3×10^{-14}	6.0	Keel (1985b)
Mkn 1419	0.0165	-19.8	S3	Sa	41.9	5.3×10^{-15}	10	This work
Mkn 461	0.0162	-20.4	S2	Sab	43.6	4.9×10^{-14}	3.0	SDSS (Thomas et al. 2013)
IRAS	0.0162	-19.5	S3	S?	53.5	3.1×10^{-15}	10	This work
14082+1347								
NGC 5548	0.0172	-20.7	S1.5	S0-a	41.0	7.3×10^{-13}	2×4	Ho et al. (1997)
Akn 539	0.0169	-19.9	S2	S?	31.9	1.3×10^{-14}	4.0	Dahari & De Robertis (1988)
NGC 7469	0.0163	-21.6	S1.5	Sa	30.2	2.9×10^{-12}	4.7	Keel et al. (1985)
NGC 7591	0.0171	-21.6	S	SBb	67.1	6.6×10^{-14}	10	This work
NGC 7679	0.0171	-21.4	S2	S0-a	59.1	1.5×10^{-14}	0.8	Gu et al. (2006)
NGC 7682	0.0171	-20.7	S1h	Sab	22.7	7.4×10^{-13}	6.0	Keel (1985a)

Note. AGN types are from NED, whose summary classes largely follow the definitions in Véron-Cetty & Véron (2006): Seyfert types 1,1.0, 1.5, 1.9, 2 are denoted S1, S1.0, S1.5, S1.9, S2, with the degree of precision of the original bibliography source used by NED. LINERs are given as S3, adding b if broad H α emission has been detected. Narrow-line Seyfert 1 is shown as NLS1. S1h denotes that broad emission lines are detected only in polarized intensity. Galaxies are ordered by right ascension, as in Kuo et al. (2008). 'Aperture' is the diameter or rectangular dimensions of the region used in measuring the [O III] flux, in arcseconds. 'Flux reference' gives the citation to the source of the adopted value of [O III] λ 5007 flux from the nucleus.

surface brightness 3.1×10^{-15} erg cm⁻² s⁻¹ arcsec⁻² within an effective area of 7.3 arcsec × 15.9 arcsec, using data from Lintott et al. (2009). Reaching this threshold allows detection of similar objects farther from the ionizing AGN, as well as objects ionized by less powerful AGN. Exposure sequences were stacked for a 5400 s total exposure in [O III] and an 1800 s total V exposure. Calibration frames were observed at the beginning of each run and standard reduction procedures were carried out using NOAO's ccdred package in IRAF5 (Tody 1986). This CCD suffered from residual bulk image (e.g. Crisp 2009), producing image persistence from bright objects which decayed with an e-folding time typically 40 min. This effect was mitigated by taking a shorter dark exposure before each new object, subtracting a smoothed and scaled version of this, as well as offsetting the telescope between the three individual 30-min exposures with the narrow-band filter. Stacking these multiple exposures also substantially rejected cosmic ray events and residual flat-field imperfections. The individual narrow-band exposures were sky-noise limited, so breaking the total observation into three exposures imposed little penalty in signal-to-noise ratio (SNR).

Continuum-subtracted (emission-line) images were produced by scaling and subtracting the combined continuum image from the combined narrow-band image. Scaling factors were determined from flux ratios of stars with known colour.

To detect spatially extended emission regions of low surface brightness, we applied several smoothing algorithms to the emission-line images. Median filtering (box size $\sim\!\!2$ arcsec square) and Gaussian smoothing ($\sigma\sim\!3.5$ arcsec) over the images improved the detectability of structure in these scales. Detection limits in [O III] emission for structures much larger than these smoothing windows are typically 2×10^{-17} erg cm $^{-2}$ s $^{-1}$ arcsec $^{-2}$.

To estimate the [O III] flux (or surface brightness) of detected objects, we establish a calibration using Landolt (1992) standard stars observed on photometric nights, along with count-rate ratios of stars between broad and narrow filters. Following Fukugita, Shimasaku & Ichikawa (1995), we converted magnitude zeropoints to total flux corresponding to one count/second within both broad-band and narrow-band filters. The ratio of stellar count rates between filters, and the filters' effective widths, let us determine the flux represented by one ADU per unit time in redshifted $\lambda 5007$ emission. This calibration factor, and the fidelity of continuum subtraction, depends on the colour of any associated continuum. Extreme colours work less well since we used only a single continuum filter, centred slightly to the red of the narrow-band filter. The emission-line flux is corrected for the wavelength-dependent filter transmission, using a correction factor equal to

⁵IRAF is distributed by the National Optical Astronomy Observatory, which is operated by the Association of Universities for Research in Astronomy (AURA) under a cooperative agreement with the National Science Foundation.

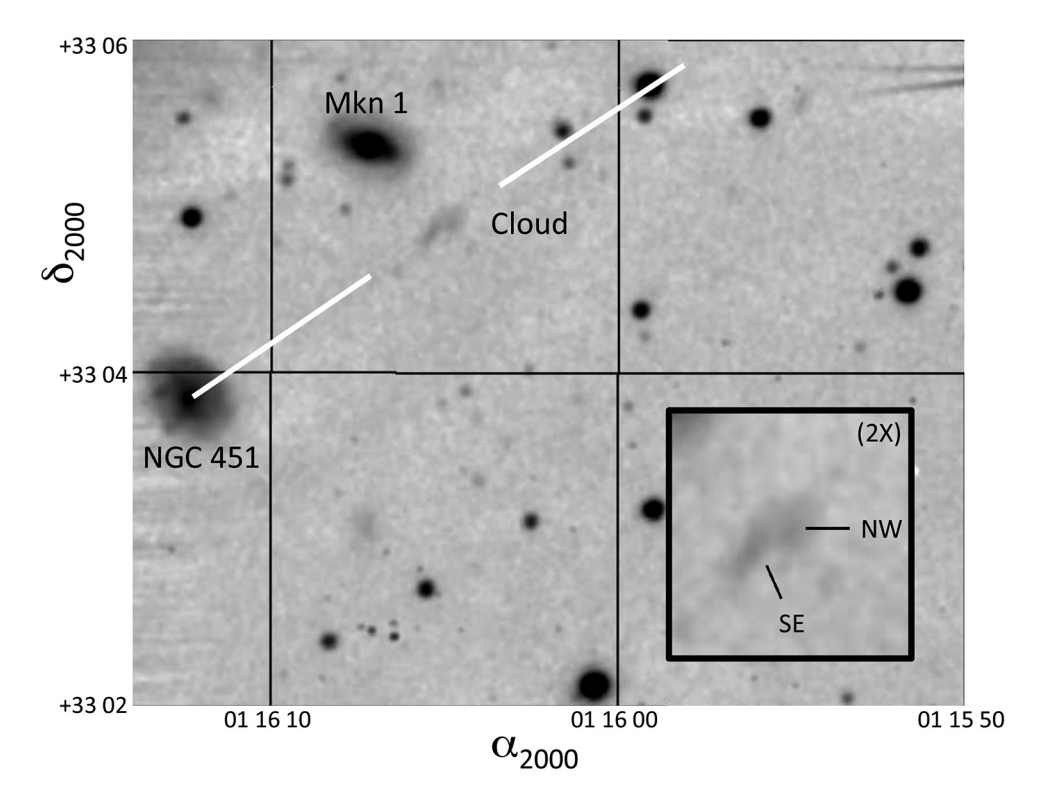


Figure 1. Stacked SARA image of the Mkn 1 field in the 510-nm narrow-band filter including redshifted [O III] emission. The newly detected ionized cloud is marked; the white bars indicate the orientation (but not length) of the slit used for both spectroscopic observations, interrupted to show the cloud clearly. This image has been smoothed with a Gaussian of 1.6 arcsec FWHM for display. The inset shows the area around the cloud enlarged by a factor of 2 from the main image, with the two regions of the cloud marked. The region shown is 240 arcsec × 300 arcsec with coordinate information from the astrometry.net service. Some faint large-scale features result from imperfect removal of reflections caused by the 6th-magnitude star HD 7578 just off the northeast edge of this image section.

the peak transmission divided by the transmission (at that z) of the 5100 Å filter. [O III] fluxes for the AGNs were measured from the emission-line images using *imexamine* from the IRAF *images* package, using a 5 arcsec initial aperture with automatic centring turned on. Three iterations were used where the image full width at half-maximum (FWHM) was fit, and the flux derived within a radius of three times the FWHM radius, while the background was fit with four times the fitting radius; this iterative procedure is intended to compensate for different image sizes in a consistent way. Flux counts for all other detected compact emission-line sources (ELDot candidates, listed in Appendix B) were calculated with automatic centring turned off and a fixed 5 arcsec fitting radius, because these objects are unresolved or nearly unresolved, by inspection.

3.2 The extended emission region near Markarian 1

3.2.1 Markarian 1 follow-up imaging

To improve our knowledge of the diffuse cloud found in our survey data, we obtained new images of Mkn 1 with SARA-KP in late 2012 and late 2016, after installation of a new imager using a nominally identical chip, operating at much lower temperature. The new camera from Astronomical Research Cameras (ARC)⁶ essentially eliminated the thermal noise that had been important in our earlier narrow-band images, and eliminated the bulk-charge afterimages.

A 3.5-h exposure stack in the same $\lambda5100$ filter goes significantly deeper, revealing structure in the cloud (Fig. 1). The image does show residuals from removal of the scattered light produced by the 6th-magnitude star HD 7578 just outside the field to the NE, which were largely reduced along with charge bleeding from other field stars by subtracting a version of the image median-filtered using a 275-pixel kernel parallel to the detector y-axis. Similar data were obtained for NGC 7591 and UGC 3995A, allowing us to reject marginal candidate detections in those field from the original survey images.

Coordinate mapping of the images, used to align multiple exposures and removing a small rotation of the camera between observations, was done using astrometric solutions with the astrometry.net web interface (Lang et al. 2010). The [O III] cloud, while irregular in form, consists largely of two components centred at 2000 coordinates $\alpha=01$ 16 05.32, $\delta=+33^{\circ}04^{\prime}\,50^{\prime\prime}.0$ and $\alpha=01$ 16 04.79, $\delta=+33^{\circ}04^{\prime}\,53^{\prime\prime}.4$, as seen in Fig. 1. We detect emission across the range of 33–45 arcsec from the nucleus, corresponding to projected distances 10.5–14.1 kpc at the adopted scale 0.315 kpc arcsec $^{-1}$. We adopt the mean of these vales, 12.3 kpc, as the characteristic distance in further calculations.

We estimated a total flux in [O III] $\lambda5007$, summing over a rectangular area 11.5 arcsec \times 22 arcsec with the longer axis in PA 304°, parallel to and centred along the spectrograph slit shown in Fig. 1. Above our detection threshold, the area of the cloud is about 141 arcsec², smaller than our summation box. The derived emission-line flux is 9.3×10^{-15} erg cm⁻² s⁻¹, giving a characteristic surface brightness within the detected area of \approx 6.6 \times 10⁻¹⁷ erg cm⁻² s⁻¹ arcsec⁻².

⁶http://www.astro-cam.com

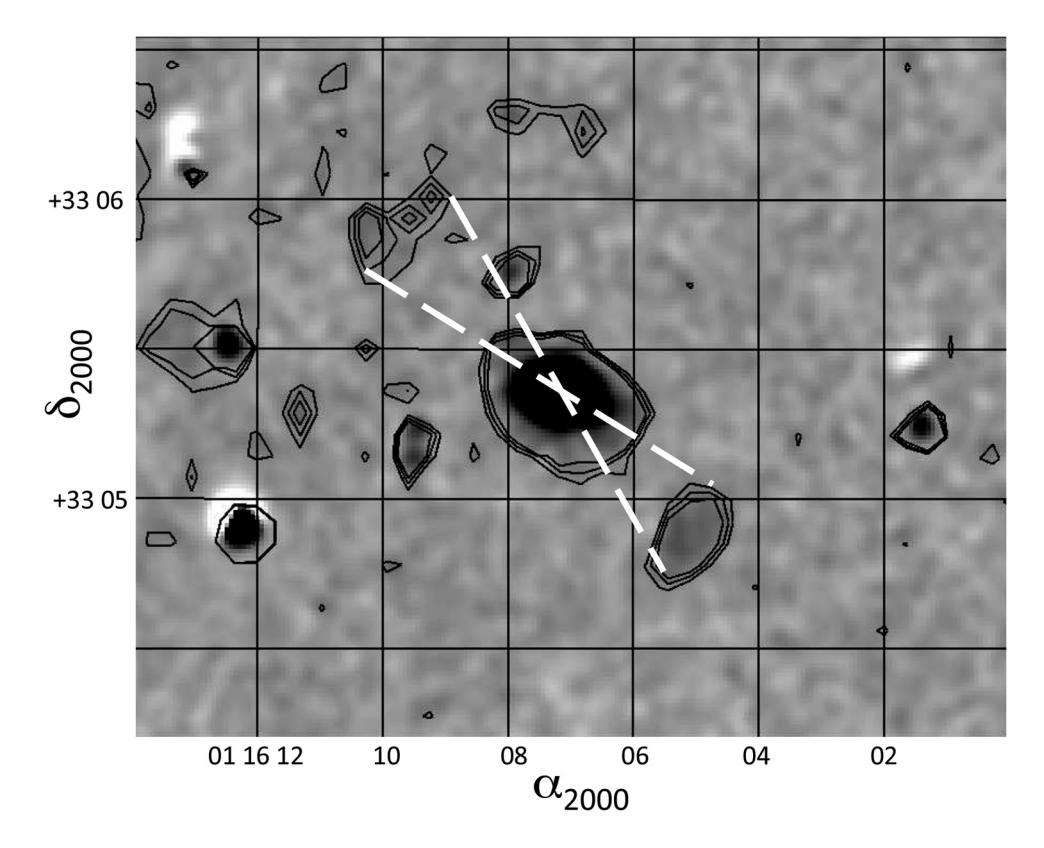


Figure 2. Byurakan H α +[NII]+[SII] image of the field of Mkn 1, using r for approximate continuum subtraction and smoothed with a Gaussian of FWHM 2.5 arcsec to emphasize faint structures. Sparse contours are overlaid to show the extent of the emission clouds, with dashed lines connecting them in notional ionization cones (full opening angle 30°) to illustrate the symmetric locations of the confirmed SW and unconfirmed NE clouds. The field shown spans 140 arcsec \times 174 arcsec with north at the top and east to the left.

Supplementary imaging of the Mkn 1 field was obtained in redshifted H α (including the adjacent [N II] and [S II] lines), via a filter centred at 675 nm with FWHM 25 nm (6000-s exposure), and the g, r continuum bands (3000 s each), using the recently commissioned CCD imager on the 1-m Schmidt telescope of the Byurakan Astrophysical Observatory (Dodonov et al 2017). After trials involving both g and r for continuum subtraction, use of the r band alone was found to give the smallest residuals near Mkn 1 and NGC 451. The subtraction has the main advantage, even for pure emission clouds, of dramatically reducing the scattered light from the bright foreground star. This image gives evidence of a fainter cloud opposite the SW one we examined spectroscopically (Fig. 2). We do not yet have additional confirmation of its existence; structure in the extended PSF of the star includes pieces of tangent arcs that would share its orientation.

3.2.2 Markarian 1 spectroscopy

To investigate the ionization source of the cloud detected near Mkn 1, we obtained a long-slit spectrum using the Kast double spectrograph (Miller & Stone 1992) at the 3-m Shane telescope of Lick Observatory, followed by an observation with the SCORPIO⁷

multimode instrument at the 6-meter telescope. Basic parameters of these data are given in Table 2. For both spectra, the slit was oriented along position angle (PA) 304° (using the standard convention measured north through east), so that when the companion galaxy NGC 451 was centered near one end of the slit, the emission cloud SE of Mkn 1 would be sampled nearly along its longest axis. For the Lick data, both NGC 451 and the emission cloud were near the ends of the slit, compromising the subtraction of night-sky emission lines. This was a particular problem for H β , because, at this redshift, its wavelength nearly coincides with that of a poorly-subtracted night-sky emission line.

BTA and Lick data allow us to analyse both (permitted) recombination emission lines (e.g. Balmer lines, He II), and forbidden lines (e.g. [S II], [N II], [O I], [O II], [O III]) from a wide range of ionization states. From studying these lines, we can characterize the ionization mechanism using BPT diagrams and the electron density and temperature through, respectively, [S II] and [O III] tracers in this galaxy. Furthermore, the detection of the He II λ 4686 line is a clear diagnostic of ionizing mechanisms typical of AGN and inconsistent with stellar photoionization, as the AGN continuum is harder than that provided by young stars (more details are given in Section 4.1).

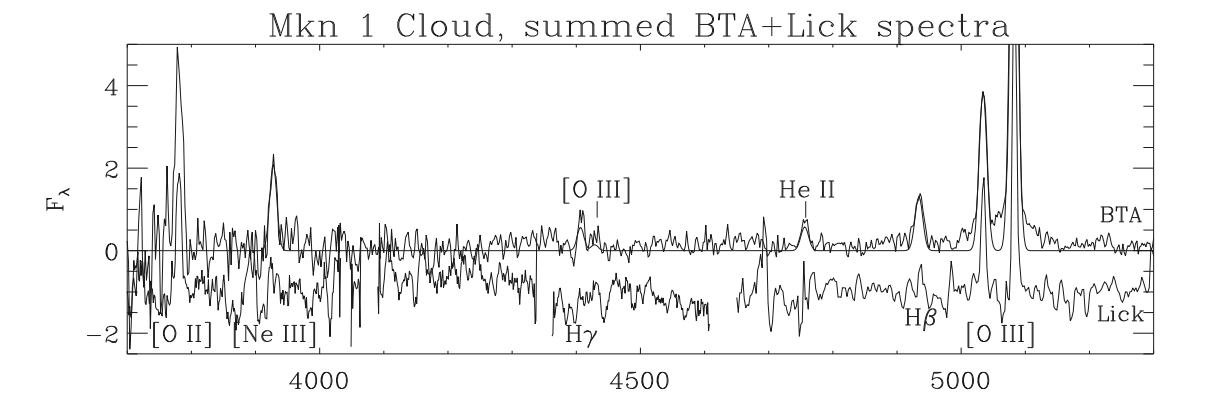
The redder member of the red [S II] doublet, $\lambda 6731$ is compromised by overlap with the atmospheric B band at this redshift, as well as a night-sky emission line. We corrected the BTA/SCORPIO

⁷Spectral Camera with Optical Reducer for Photometrical and Interferometrical Observations, Afanasiev & Moiseev (2005).

⁸BTA, the abbreviation for Bol'shoi Teleskop Azimutal'nyi or Large Altazimuth Telescope, https://www.sao.ru/Doc-en/Telescopes/bta/descrip.html of the Russian Academy of Sciences.

Table 2. Spectroscopic observations.

Spectrograph	Lick/Kast blue	Lick/Kast red	BTA/SCORPIO
UT date	2013 January 14	2013 January 14	2017 August 17
Exposure time (s)	7200	7200	7200
Slit width (arcsec)	2.0	2.0	1.0
Wavelength range (Å)	3669-4595	4657-7409	3757-7223
Pixel sampling (Å)	1.264	2.32	2.00
Angular pixel scale (arcsec)	0.43	0.43	0.357
FWHM resolution (Å)	5.6	6.2	12.6



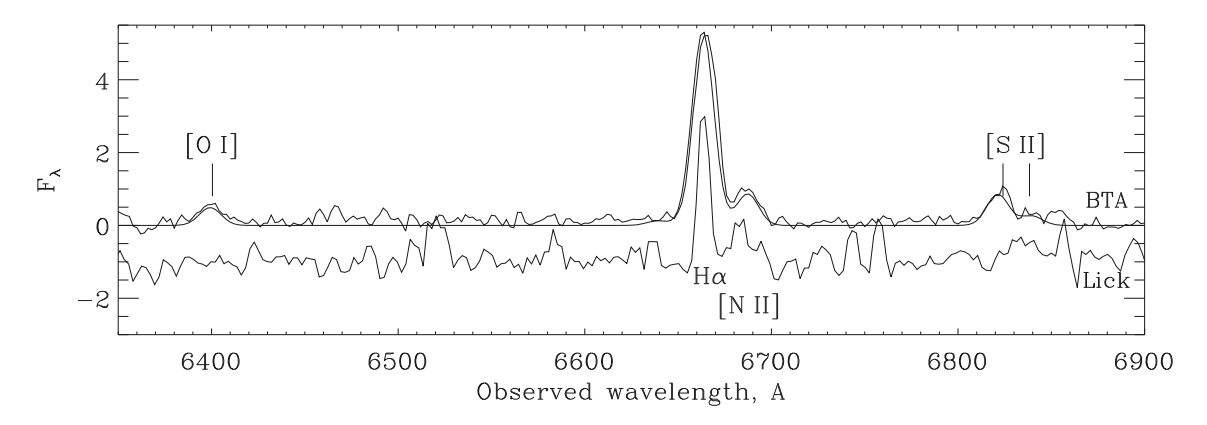


Figure 3. Optical spectra of the Mkn 1 cloud, summed over a 23 arcsec region along the 1 arcsec slit. The vertical scale, in units of 10^{-17} erg cm⁻² s⁻¹ Å⁻¹, truncates the peak of $[O III] \lambda 5007$ to show other lines more clearly. That line is 2.93 times as strong as the $\lambda 4959$ line in energy units (Tayal & Zatsarinny 2017). He II $\lambda 4686$ is clearly detected. The location of the weak, temperature-sensitive $[O III] \lambda 4363$ line is marked. The sum of single Gaussian fits to the emission lines in the higher-S/N BTA data is overplotted. The Lick spectrum is shown, offset below the BTA data by 10^{-17} erg cm⁻² s⁻¹ Å⁻¹, after 6-Å boxcar smoothing. The Lick data are rescaled to account for the resolution difference (for blue and red segments separately) to give similar peak heights for narrow emission lines, and were not corrected for telluric *B*-band absorption affecting the [S II] doublet. Wavelengths contaminated by Hg night-sky lines are omitted. For clarity, only the fits to the narrow components of the [O III] lines are shown.

data for B-band absorption using the spectrum of a hot star along the slit, and explored several fitting routines to correct for residual night-sky variations along the slit. The uncertainty range on the $\lambda 6717/\lambda 6731$ ratio is still >1.40, allowing only values close to the low-density limit. The [O II] $\lambda\lambda 3726,3729$ doublet in both data sets lies in a region where the system sensitivity is low, giving a signal-to-noise ratio too low for an independent density estimate.

Combination of the observed lines from H, He, N, S, and especially three ionization levels of O, can specify the ionization mechanism, density, and composition of the material. Among weaker emission lines, the signal-to-noise ratio of the BTA/SCORPIO data is sufficient to measure He II emission well, constraining the slope

of the ionizing continuum, and (marginally) detect [O III] $\lambda4363$ for an electron-temperature measurement.

Fig. 3 shows the cloud spectrum summed along 65 spatial pixels (23 arcsec). We measure line fluxes by fitting single Gaussian components to each strong line; the fitting routine was constrained to fit a single FWHM for the set of [O III], H β , H γ , He II, and separately the red lines H α , [N II], [S II], [O I]. The resulting FWHM values were (including the instrumental width) 850 (650) km s $^{-1}$ in the blue, and 610 (240) km s $^{-1}$ in the red for the BTA (Lick) integrated spectra. The very different linewidths for the red lines reflect the higher resolution of the Lick red data. This simple prescription fits well except for the underlying

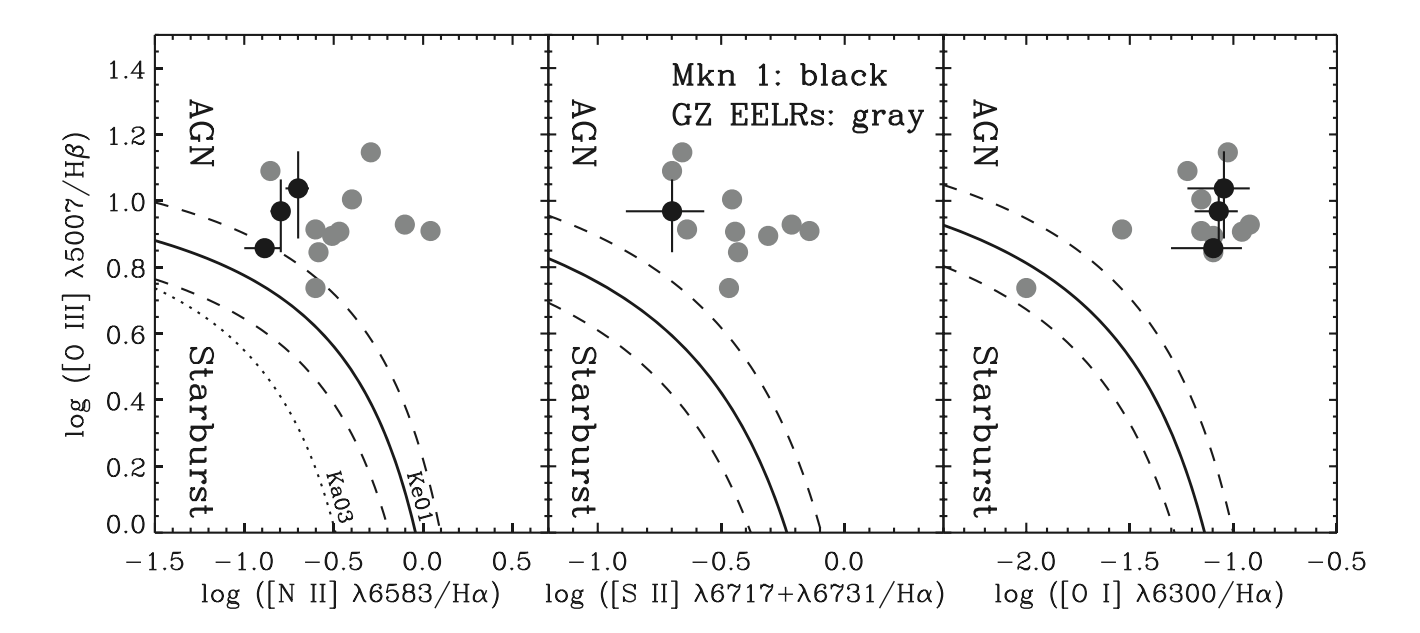


Figure 4. Location of the Mkn 1 cloud (black points, with error bars) and Galaxy Zoo EELR clouds (grey points) in three common BPT diagrams. For the two diagrams where separate measurements are given in Table 3, the top black data point shows the SE cloud, while the bottom shows the NW cloud, with the overall mean in the middle. The solid curves show the boundary between extreme starbursts and AGNs (Kewley et al. 2001), with dashed curves showing the ± 0.1 dex theoretical uncertainty from their work, marked Ke01. For the first diagram, we add a dotted curve showing an empirical demarcation (Kauffmann et al. 2003), marked as Ka03. To reduce clutter, we do not show the AGN/LINER boundary, which lies below all the points in these samples.

Table 3. Mkn 1 extended cloud: spectroscopic emission-line ratios.

Line ratio	Lick integrated	BTA: integrated	SE cloud	NW cloud	Mean GZ EELR
[O II] \(\lambda 3727/[O III] \(\lambda 5007\)	0.42 ± 0.11	0.39 ± 0.05	0.43 ± 0.07	0.50 ± 0.07	0.51
$[O III]\lambda 5007/H \beta$	_	9.3 ± 2.3	10.9 ± 3.2	7.2 ± 3.4	8.38
$[O III]\lambda 5007/H \alpha$	2.40 ± 0.3	2.2 ± 0.3	2.8 ± 0.4	1.5 ± 0.3	2.74
$H \alpha / H \beta$	_	4.2 ± 1.0	3.8 ± 1.4	4.9 ± 1.4	_
[Ν II]λ6583/Ηα	0.18 ± 0.08	0.16 ± 0.02	0.20 ± 0.03	0.13 ± 0.03	0.43
[Ο Ι]λ6300/Η α	_	0.085 ± 0.02	0.09 ± 0.03	0.08 ± 0.03	0.071
He II λ 4686/H β	_	0.43 ± 0.06	0.61 ± 0.12	0.28 ± 0.12	0.30
[Ne III] λ3869/ [O II] λ3727	_	0.39 ± 0.09	0.40 ± 0.12	0.48 ± 0.12	0.33
[S II] λ6717 / λ6731	_	$>1.40(2\sigma)$	_	_	1.35
[S II]/H α	_	0.20 ± 0.07	_	_	0.46

Note. For each data set, columns 2 and 3 report the line ratios integrated along the slit for the detected extent of the cloud. Columns 4 and 5 give the ratios for the two portions of the cloud identified morphologically and kinematically. 'Mean GZ EELR' is the mean value of each ratio for the set of extended emission-line regions found in the Galaxy Zoo (GZ) survey, using data from Keel et al. (2012a).

broader component of the $[O\,{\sc III}]$ lines (which will be discussed in Section 4.4).

4 MARKARIAN 1 AND ITS DISTANT IONIZED CLOUD

4.1 Ionization

Our initial Lick spectrum showed the cloud to have high ionization, but left the ionizing mechanism ambiguous. The deeper BTA data show He II emission at a level requiring an AGN continuum if photoionized, and also show that the electron temperature and line widths are low enough to strongly disfavour shock ionization (as discussed below). This object is an instance of low-metallicity gas whose location in the most commonly used BPT (Baldwin, Phillips & Terlevich 1981) diagram (Groves, Heckman & Kauffmann 2006), which plots $[O III] \lambda 5007/H \beta$ versus $[N II] \lambda 6583/H \alpha$, is

close enough to the starburst boundary to benefit from additional classification criteria. For this reason, detection of He II emission has been important in establishing the ionizing source of extended clouds seen near galaxies, showing in some cases the presence of either obscured or fading AGN (Lintott et al. 2009; Keel et al. 2012a; Schweizer et al. 2013; Keel et al. 2019). The Mkn 1 SW cloud falls in regions of the low-metallicity classification diagrams for [O III]/H β and [O III]/[O II] versus [N II]/[O II] of Groves et al. (2006), indicating AGN ionization. It also falls in the AGN region of the BPT-[O I] diagram of [O III]/H β versus [O I]/H α (Baldwin et al. 1981; Kewley et al. 2006). We show this in Fig. 4, comparing the individual NW and SE components of the Mkn 1 cloud (and the mean) to the spatial averages of EELR clouds from the Galaxy Zoo sample (Keel et al. 2012a) in the three most commonly used BPT diagrams.

Table 3 shows emission-line ratios integrated along the slit for the entire cloud, and for the two subregions suggested by peaks in the narrow-band image (Section 3.2 and Fig. 1). Since the Gaussian fitting we used to measure line fluxes is a non-linear process, adjusting both positions and widths of emission peaks after manual input of initial guesses, we used an empirical approach to estimate uncertainties in the results. We repeated the fitting of blue and red spectra segments a number of times, interactively adding additional lines to be fit at wavelengths selected arbitrarily in continuum regions, fitting the spectrum repeatedly and adding \approx 5 such fictitious components at a time, so the strong emission lines would constrain the line width in the same way as for fits with only genuine emission lines. We took the scatter in the fitted properties of these fictitious lines as an estimate of the expected flux error in each segment of each spectrum. For the red lines, this process was also repeated to include changing the interpolation order of sky subtraction (since the redshifted [S II] lines are at wavelengths affected by OH airglow features). Modest differences in ionization properties are found between the NW and SE regions, with the SW part of the cloud more highly ionized, as seen in $[OIII]/H\beta$ versus [N II]/H α and He II/H β . Good agreement is seen between integrated line ratios from our two sets of spectral data.

As noted in Section 3.2.2, estimating the electron density using the [S II] $\lambda\lambda6717,6731$ lines required correction for telluric *B*-band absorption. Following the procedure outlined above, we estimate errors from fits of fictitious Gaussian lines at random adjacent wavelengths, in this instance constrained to match the stronger [S II] line in width. The resulting limit for the $\lambda6717/\lambda6731$ intensity ratio is >1.40 at the 2σ level, leading to a 2σ density limit $n_{\rm e} < 26~{\rm cm}^{-3}$, using the IRAF task *temden* (Shaw & Dufour 1995) and assumed temperature 10^4 K. The corresponding limits at the 3σ level are I($\lambda6717$)/I($\lambda6731$) > 1.08, $n_{\rm e} < 430~{\rm cm}^{-3}$. In this range of line ratios, our uncertainty range gives only broad information on the density.

The [OIII] $\lambda4363$ line is marginally detected (formally at the 2σ level, at intensity 0.016 times that of the $\lambda 5007$ line) in the cloud integrated spectrum (Fig. 3). This lets us place an upper limit on the electron temperature via its ratio with the $\lambda 5007$ line. Using the temden task in the nebular package within IRAF (Shaw & Dufour 1995), we place a 3σ bound $T_{\rm e} < 20~000~{\rm K}$ for low electron density ($n_e < 50 \text{ cm}^{-3}$ as is typical for such distant AGN clouds; Lintott et al. 2009; Keel et al. 2012a). This temperature, too low for shocks to match the ionization level found from [O III]/H B and He II/H β , points to photoionization by an AGN continuum as the ionizing agent for this cloud. The line ratios are very similar to those observed in the EELRs studied in the Galaxy Zoo sample (table 4 of Keel et al. 2012a), whose mean values are shown in the last column of Table 3. These objects, and the data on supernova remnants compiled in that paper, furnish a useful illustration of how shock ionization, clearly dominant in the selected supernova remnants, has a higher characteristic electron temperature at the relevant ionization levels than does AGN photoionization. Electron temperatures in the supernova remnants range from 20 000 to 69 000 K, [O III] $\lambda 4363/\lambda 5007 = 0.035-0.115$. However, He II $\lambda 4686$ is detected in only a small fraction of those observations, with a median value He II/H $\beta = 0.08$ even among detections, compared to the mean value of 0.30 in the Galaxy Zoo EELR sample (which contains no upper limits).

As shown in Fig. 3, the higher S/N BTA spectrum reveals the presence of a broad component underlying the $[O\,III]\lambda\lambda4959,5007$ emission lines. A simple Gaussian decomposition suggests that this broad component may have as much as 0.3 times the flux of the prominent narrow lines, with a line width corresponding to 5600 km s⁻¹ at half peak (although we use a two-component Gaussian fit for convenience of description, our data have insufficient SNR to say

whether this broad component's profile is in fact close to a Gaussian. We consider possible scattering origins for this line component in Section 4.4.

4.2 Relation to circumnuclear gas and HI

Stoklasová et al. (2009) present integral-field spectroscopy of the central regions of Mkn 1, showing resolved emission lines across a region spanning about 20 arcsec along the projected major axis of the inner disc of Mkn 1. They identify narrow high-ionization regions to NE and SW. To specify the locations of the ionization cones, we take a criterion [O III]/H β > 9.2 from their fig. 13. Outside the nuclear emission extending to about r=4 arcsec (1.3 kpc), the possible ionization cones are seen as far as 2.4 kpc from the nucleus between position angles 50° – 85° with the highest ionization along PA 65° , slightly misaligned with the stellar distribution.

Archival *Hubble Space Telescope* images (Pjanka et al. 2017) show the inner disc to be elongated along PA 72° , with numerous star-forming regions most prominent on its south and western sides (contributing strongly to the Balmer H α and H β flux maps from Stoklasová et al. 2009).

The distant cloud we have found to the southwest is projected at radii from 33 to 45 arcsec (10.5–14.1 kpc) and spans PA 207° – 236° , while the inner possible ionization cone on this side spans 230° – 265° , barely overlapping (as shown in Fig. 5). If both structures are ionized by radiation in a fixed conical pattern, neither structure samples most of the cone width. This might mean that the inner disc gas and the outer H I structure are misaligned with each other and thus intercept different portions of the ionizing radiation pattern. Alternately, precession of the ionizing pattern on time-scales giving appreciable offsets on the light-traveltimes between inner ionization cone and the distant emission cloud ($\approx 3 \times 10^4$ yr) could produce this offset

The highest resolution available H I data are the GMRT results from Omar et al. (2002), with beam size 27 arcsec \times 31 arcsec FWHM. Fig. 5 schematically shows the locations of the southwest and possible northeast emission clouds compared to their H I contours. The confirmed SW cloud falls right at the outer edge of the H I structure, possible associated with an inflection of declining surface density, while the possible NE cloud falls largely in the gap between the two H I features in that side. We might speculate that this is similar to the location of Hanny's Voorwerp in a gap in the H I tail of IC 2497 (Józsa et al. 2009), where ionization of most of the gas creates a gap in the H I structure. Fig. 5 also illustrates how the outer clouds and inner ionization cones overlap only partially in orientation around the nucleus.

4.3 Kinematics

We examine the radial-velocity structure of the cloud by using wavelength peaks as retrieved from single-Gaussian fitting of the two components of the [O III] doublet, constraining both $\lambda\lambda4959,5007$ lines to have the same width (see Section 3.2.2). The results show a velocity gradient the detected extent of the cloud. The velocity gradient in both Kuo et al. (2008) and Omar et al. (2002) H I data sets is much shallower than we see in optical emission, roughly 10 km s⁻¹ across the entire emission-line cloud, due to their significant beam smoothing (equivalent circular beam sizes are roughly 29 arcsec FWHM for the Omar et al. 2002 data and 57 arcsec for Kuo et al. 2008, both larger than the entire extent of the SW emission-line cloud). In view of our typical uncertainty of order 30 km s⁻¹, either a single roughly linear velocity gradient, or a stronger gradient

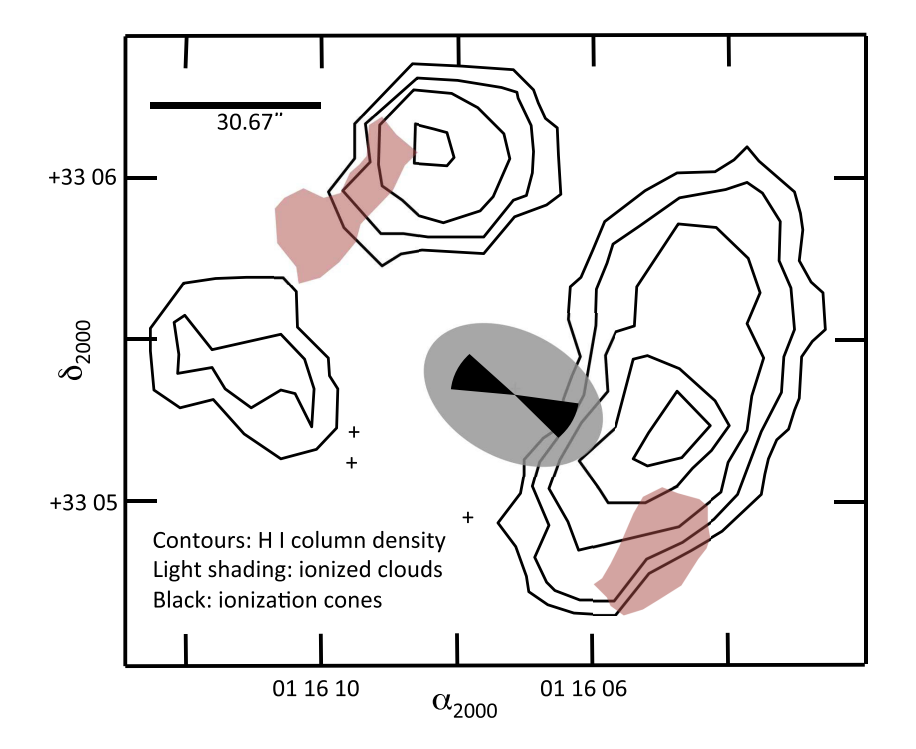


Figure 5. Locations of the emission-line clouds, shown shaded in light red within the lowest contours from Fig. 2, and H1 column-density contours taken graphically from fig. 5 of Omar et al. (2002), aligned using the star positions shown by crosses. Contour levels are $(0.3, 0.8, 1.3, 2.3, 3) \times 10^{20}$ cm⁻². The ellipse shows the optical disc of Mkn 1, within much of which H1 emission is hidden by absorption against the AGN continuum source. North is at the top and east to the left. The scale bar indicates the major axis of the synthesized H1 beam, which has FWHM dimensions 30.67 arcsec \times 27.28 arcsec, elongated in position angle 100° . The black zones within the schematic disc show the extent of the ionization cones studied by Stoklasová et al. (2009), and their partial misalignment with the more distant clouds we have identified.

in the SE section plus a constant velocity for the NW half, fit the optical data equally well (Fig. 6). A linear χ^2 -minimization fit gives a gradient -3.7 ± 1.6 km s⁻¹ arcsec⁻¹, with reduced $\chi^2 = 1.82$ for 2 degrees of freedom (DOF). A two-piece linear fit gives gradients $-8.5 \pm 4.1 \text{ km s}^{-1} \text{ arcsec}^{-1}$ for slit location <12 arcsec as in Fig. 6, and $-1.0 \pm 3.1 \text{ km s}^{-1} \text{ arcsec}^{-1}$ for slit location >12 arcsec. This more complex fit has reduced $\chi^2 = 2.00$ for 5 DOF, since the break location was also a fitted parameter. The modest difference $\Delta \chi^2 =$ 0.18 between the two cases may be best interpreted as indicating that our data do not require a two-component fit, although oneand two-component fits are nearly equivalent in goodness. These fits are overplotted on Fig. 6. Both H I studies give a somewhat higher heliocentric velocity in this region as shown in the figure. Again, their limited spatial resolution limits interpretation of the kinematic comparison beyond this note. When an AGN ionizes surrounding gas without exerting a strong kinematic influence, such as in outflows, it offers the opportunity to trace its velocity structure at much higher resolution than is currently feasible with H I alone.

4.4 Broad [O III] wings and scattering?

We can compare the cloud spectrum with the (blue) nuclear spectrum obtained by Balick & Heckman (1979), shown together in Fig. 7. While the nucleus does have broad wings to [O III], the ones shown in the cloud are roughly twice as strong as a fraction of total [O III] flux. Scattering of light from the narrow-line region (NLR) by dust in the distant cloud cannot be a dominant contributor to the spectrum, because of the differences in He II/H β and [O II] λ 3727/[O III] λ 5007 line ratios. Pure scattering would

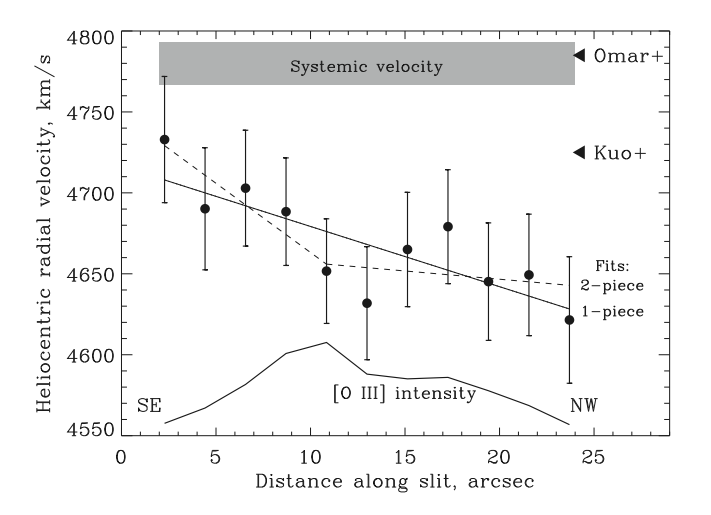


Figure 6. Radial–velocity structure of the Mkn 1 cloud along the BTA spectroscopic slit, evaluated by Gaussian fits to the [O III] lines integrated over 2-arcsec regions. Errors are derived from differences between line measurements as a function of line flux. The continuous curve at the bottom shows the intensity of [O III] emission, illustrating how the two structural components may have different velocity gradients. The single full line and broken dashed lines show the one- and two-component χ^2 fits described in the text. The systemic velocity and its uncertainty range are marked as derived from H1 by Omar et al. (2002); optical results fitting across the disc give the same value with somewhat smaller error. The triangles indicate the radial velocities derived from H1 in this region by Omar et al. (2002) and Kuo et al. (2008), with a beam smoothing larger in each case than the extent of this graph. Distance along the slit increases from southeast to northwest.

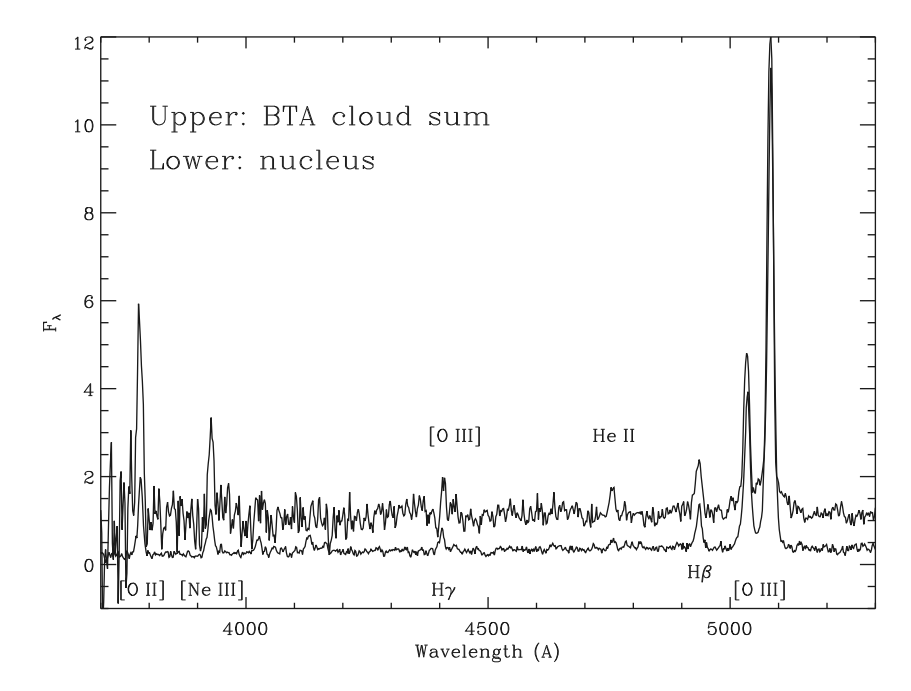


Figure 7. Comparison of blue spectrum of the Mkn 1 cloud (integrated BTA spectrum as in Fig. 3) with the nuclear spectrum from Balick & Heckman (1979). The nuclear spectrum has been rescaled to match the [O III] intensity peak of the cloud for ease of comparison. As noted in the text, the most obvious differences are that the cloud shows higher He II/H β , lower [O II] λ 3727/ [O III] λ 5007, and relatively stronger broad wings on the [O III] doublet. The flux is in units of 10^{-17} erg cm⁻² s⁻¹, and the cloud spectrum is offset upwards by one of these units for clarity.

change line ratios only by the change in scattering-cross-section across the wavelength difference between the lines, which is particularly inconsistent with the relative strengths of the emission lines between spectra of the nucleus and cloud. Most obviously, He II/H β is larger in the cloud, while [O II] $\lambda 3727/[O III] \lambda 5007$ is smaller in the cloud. These changes go in opposite senses with wavelength, while dust scattering across the optical uniformly makes the light bluer and scattering by free electrons maintains the same spectral shape due to the wavelength independence of the Thomson cross-section. Similarly, but less well constrained, we see no evidence of scattered light from any presumed broadline region (BLR), based on lack of broader components to the Balmer lines (especially $H\alpha$, where any broader component must be substantially weaker than the wings we observe for [OIII]). Spectropolarimetry by Kay (1994) did not detect a polarized signature of the BLR in Mkn 1. Likewise, in this object Veilleux, Goodrich & Hill (1997) found no signature of an obscured BLR in near-IR spectroscopy. The strongest lines in their spectra, Br γ and H₂ λ2.121 μm, lack the blue wing seen in the strongest optical emission lines from the nucleus. Both these observations suggest that the broad component at [O III] is not scattered from the central region, unless its spectrum changes strongly with viewing angle or time.

4.5 Energy budget and AGN history

In principle, the ionization level of outlying EELR gas samples the past luminosity of the AGN. We follow the approach of Keel et al. (2012a) to estimate the minimum AGN luminosity needed to power the distant cloud, and compare with the obscured AGN luminosity (since Mkn 1 is a Type 2 Seyfert, this is appropriate).

The cloud's H β surface brightness⁹ and projected distance 12.3 kpc from the nucleus require an ionizing luminosity $>10^{43}$ erg s⁻¹, by a factor depending on the clumpiness of the gas (and through this, ultimately connected to its optical depth at the Lyman limit). Using the 2σ (3 σ) upper limits to the electron density from the [SII] lines $n_e < 26$ (430) cm⁻³ can give complementary upper limits to the ionizing luminosity. Following Komossa & Schulz (1997), the ionization parameter U derived from the line ratio [OII]/[OIII] = 0.39 (Table 3) and a typical AGN continuum shape is U = 0.002. The emission rate of ionizing photons is $Q_{\rm ion} = U \times (4\pi r^2 n_{\rm e})$, where r is the distance from AGN to the gas cloud and n_e is the cloud's electron density, so for r =12.3 kpc and the two n_e limits, $Q_{ion} < 2.8 \times 10^{53} \, (4.6 \times 10^{54})$ photons s⁻¹. For a generic AGN continuum, the mean energy of ionizing photons is roughly 2 Rydbergs, so this becomes L_{ion} $< 1.3 \times 10^{43} (2.1 \times 10^{44}) \text{ erg s}^{-1}$. These two approaches give bounds on the ionizing luminosity seen by the cloud at the epoch of the emitted photons. The derived value is $1.5 \pm 0.6 \times 10^{43}$ $erg s^{-1}$.

We estimate the far-infrared luminosity using the IRAS-based FIR parameter (Fullmer & Lonsdale 1989), which gives a good estimate of the total luminosity from 42 to 122 μm for a wide range of spectral shapes. Predominantly from reprocessed UV radiation, this total is 1.7×10^{44} erg s $^{-1}$. A more complete accounting includes the ionizing radiation reaching gas before being intercepted by grains. The narrow [O III] $\lambda 5007$ lines in AGN typically account for a fraction 1/3500 (Heckman et al. 2004) to 1/1500 (Netzer 2009) of the bolometric luminosity, including typical correction for internal attenuation. For a typical continuum shape as measured

⁹Using a recombination line to count ionizing photons most directly, independent of details of the ionization balance.

in luminous AGN (Elvis et al. 1994), the ionizing luminosity accounts for a fraction 0.32 of the bolometric luminosity (although these scaling factors will have considerable scatter for individual nuclei). The nuclear spectrum obtained by Balick & Heckman (1979) gives an observed flux $F_{5007} = 5.4 \times 10^{-13}$ erg cm⁻² $\rm s^{-1}$, which implies an [O III] luminosity $3.0 \times 10^{41} \rm \ erg \ s^{-1}$. Using the scaling from Heckman et al. (2004) to be more conservative in testing for AGN variation over the light-traveltime to the SW cloud, we find the continuum fraction reaching the gas to be energetically dominant over that intercepted by dust, accounting for an ionizing luminosity $3.4 \times 10^{44} \text{ erg s}^{-1}$, giving a total L_{ion} $=5.1 \times 10^{44} \text{ erg s}^{-1}$. This is sufficiently greater than the ionizing requirements for the cloud (1.5 \pm 0.6 \times 10⁴³ erg s⁻¹) to make it plausible (although not required) that the AGN has maintained a roughly constant output over the light-traveltime to the clouds $(\approx 40\ 000\ vr^{10})$.

5 SAMPLE IMPLICATIONS FOR AGN CONE ANGLES AND EPISODE DURATIONS

In this section, we give a simple calculation of the typical width of ionization cones for the whole sample, under some simplifying assumptions. These are (1) that all the AGNs are powerful enough to ionize observable clouds in the H I structures and (2) that these structures are reasonably approximated as great-circle arcs viewed from each AGN. We estimate the ionizing luminosity of each AGN, constructed from the far-IR and nuclear [O III] luminosities as done in Section 4.5 for Mkn 1.

We used the published H I column-density maps from Kuo et al. (2008) to estimate the angle L spanned by separate H I features around each AGN, approximated as tangential arcs (Table 4). These values are intended to apply to features outside the host discs, which are at greater distances (sampling longer light-traveltimes) and less likely to be in the host disc planes and therefore shielded by each galaxy's own neutral hydrogen. Expressions for the chances of randomly distributed arcs and (bi)cones intersecting are derived in Appendix A. Applying this derivation to the ionization of AGN EELRs implicitly assumes that the AGN has constant luminosity (in practice, that it is luminous for a time much longer than the light-traveltime from the AGN to the gas). If, instead, the AGN is luminous in episodes comparable to this time, or even shorter, the derived cone angles will be too small, since fewer AGN will both ionize the gas and be observed at high luminosity. At this exploratory point, our aim is not to establish the duration if it is short, but to ask whether this sample provides evidence on AGN episode lengths or not. We do this by comparing the cone radii needed to account for our result (one EELR in our sample) with typical cone radii seen in nearby AGN. A substantially narrower computed value here could be evidence of episodic AGN activity on the light-traveltime-scales between sample AGN and the H I features (typically 100 000 yr for the H I features detected by Kuo et al. 2008).

Rather than extended H I discs or tidal tails around the AGN hosts themselves, most of the nearby H I structures in this sample are associated with companion galaxies, with H I redshifts making physical association very likely. In this light, this survey is largely a search for AGN cross-ionization as defined by Keel et al. (2019),

Table 4. Extended H I structures.

Field	r _{proj} (kpc)	L (°)	$L_{\rm ion}$ (erg s ⁻¹)	$A_{ m half}$ $(^{\circ})$
NGC 7469	24.7	120	1.8×10^{45}	31.9
NGC 5548-1	54.5	23	5.0×10^{44}	53.0
NGC 5548-2	80.5	15	5.0×10^{44}	55.3
NGC 5548-3	20.9	79	5.0×10^{44}	39.1
Akn 539	54.1	77	8.6×10^{42}	39.5
NGC 7679	62.3	72	1.0×10^{43}	40.5
NGC 7682	62.3	52	5.0×10^{44}	45.1
Mkn 461	58.9	26	3.0×10^{43}	52.0
MS 04595+0327	47.4	36	8.9×10^{43}	49.4
UGC 3157	68.5	26	3.6×10^{42}	52.0
Mkn 993	82.2	16	2.6×10^{44}	55.2
NGC 513	47.4	57	1.2×10^{44}	44.0
Mkn 1	62.3	74	5.1×10^{44}	40.1
NGC 1167	82.2	8.2	1.8×10^{43}	57.5
UGC 1395	52.1	31	4.2×10^{43}	50.7
Mkn 573	75.4	10	6.4×10^{44}	56.9
Mkn 1157	41.9	20	1.1×10^{44}	53.9
NGC 7591	50.0	26	4.5×10^{43}	52.0
NGC 841	109	24	7.8×10^{41}	52.8
Mkn 341	76.0	12	6.0×10^{42}	56.2

Notes. The observed H1 regions are projected at distances r_{proj} from the nuclei. A_{half} is the angle where $P(A,L)=\frac{1}{2}$ as derived in Appendix A, meaning the median radius of an ionization cone whose probability of intercepting randomly oriented arcs of gas spanning the observed angle L (column 3), as measured on H1 maps, is $\frac{1}{2}$. The ionizing luminosities L_{ion} are estimated as described in the text.

using companion galaxies to sample the emerging radiation independent of biases due to the gas distribution within the AGN host galaxies. Projection factors in these cases are poorly constrained, with no necessary connection to the AGN host inclination. In view of this, we considered examination of projection effects based on the inclinations of the remaining hosts (Akn 539, IRAS 05078+1626, IRAS 14082+1347, Mkn 352, Mkn 359, Mkn 1040, NGC 266), but as this would affect only 30 per cent of the entries in Table 4, the outcome is still dominated by the behaviour of gas around companion galaxies. In this table, using the nomenclature in Appendix A, L is the arc length of H I features outside the galaxy disc as measured about the nucleus, and A is the radius (angular half-width) of the ionization cone. The median value of A, denoted A_{half} , is calculated as the value such that the odds of the bicone intercepting randomly oriented gas arcs are equal for larger or smaller A.

The broader the cones of escaping ionizing radiation, the greater the chance of encountering a given H I structure, so the larger the expected number of ionized clouds in a sample with known H I properties. In the other direction, luminous AGN episodes, with time-scales shorter than the light-traveltimes from the AGN to the clouds, would reduce the number of ionized clouds for a given cone angle by a factor related to the duty cycle of the luminous phases. For the entire sample, the number of detections - only one (Mkn 1) for the observed arc angles - suggests narrow cones of escaping ionizing radiation, typically 10° half-width. In contrast, by modelling 17 well-observed cases, Fischer et al. (2013) find a median half-opening angle 40° (full width 80°). This is so much broader than the typical value we derive from our low detection rate that intermittent luminous episodes may be required to reconcile the two values. An estimate of the error range on this, fitting roughly with Poisson statistics, would be the limit corresponding to a number

¹⁰The light-traveltime between the AGN and the cloud we have observed, in the plane of the sky.

of detections ≤ 2 , which gives half-width $<16^{\circ}$ for this sample (full width $<32^{\circ}$). The derivation in Appendix A incorporates the case of a single object with both cones intercepting a gas arc, so these values do not change if the second cloud in Mkn 1 is confirmed.

This conceptually clean formulation runs into several complications in actual data, so our results also provide an outline of ways to improve this approach. Projection effects can increase or decrease measured arc lengths, and could render an arc of gas more like a radial spur or blend it with the host galaxy disc. The limited angular resolution of the current H I data often blend external structures, to some extent, with the host disc gas. Finally, shadowing of some of the H I by material in the inner disc or AGN torus will often prevent ionizing radiation from escaping in both the planes (broadened if either one is warped or twisted; Lawrence & Elvis 2010). Our primary interest is in ionized gas outside the normal disc interstellar medium of the host galaxy; a sufficiently warped disc could escape the self-shielding of the inner regions. Lacking a prescription for a fuller treatment, we present the results as is with these cautionary notes.

6 CONCLUSIONS

We have surveyed the environments of a set of Seyfert galaxies with known H I structures, using a narrow-band [O III] filter, in search of distant nebulosities photoionized by the AGN (EELRs). Among 26 Seyfert galaxies with H I observations by Kuo et al. (2008), we found an EELR in only one case (Mkn 1). Among the 18 galaxies with extended H I beyond the galaxy discs, there are 20 discrete, outlying H I regions (Table 4), projected 20–76 kpc (65 000–250 000 light-years) away from the nearby Seyfert nuclei. The lack of observed photoionization in all but one of the outlying H I regions indicates intermittent luminous episodes may occur on time-scales of less than 20 000-50 000 yr. This follows from our derivation of the likelihood that a bi-cone of half-opening angle A will intersect an arc of angular length L, which we then apply to our sample of 18 AGNs. Here, L is the measured, projected size of the outlying H I region, and A sweeps out a theoretical cone of ionizing radiation emerging from a galactic nucleus. Our observed case, where only 1 of the 20 associated H I features is intersected by the bi-cone, gives $A \approx 16^{\circ}$. Given that observed opening angles of ionization cones are typically twice this value, our results therefore suggest that photoionizing radiation leaving at least some of the Seyfert nuclei in this study has not yet reached the outlying H I regions. The luminous episode we currently observe at the nucleus began so recently that its radiation has not reached the H I structures (at projected distances 65 000–250 000 light-years). The primary assumption in reaching this conclusion is that the AGN in our sample are luminous enough to ionize gas at these distances, which is supported by the nuclear luminosities mostly 10^{43} – 10^{45} erg s⁻¹ (Table 4), and by the example of Mkn 1.

Mkn 1 is accompanied by a large emission-line region projected 12 kpc from the AGN, for which spectroscopy confirms that it is photoionized by the AGN itself. Radial velocities support an association between this material and the larger extended H I disc. The location of this ionized region does not match the ionization cone inferred from circumnuclear gas, suggesting either that neither emission region fully crosses the escaping cone of radiation or that the cone of radiation moves on time-scales $\approx\!\!40\,000$ yr. A fainter emission-line cloud may appear on the opposite side of the galaxy, but interference from a very bright foreground star leaves this detection tentative.

ACKNOWLEDGEMENTS

The observations at the 6-m telescope of the Special Astrophysical Observatory, Russian Academy of Sciences, were carried out with the financial support of the Ministry of Science and Higher Education of the Russian Federation (including agreement No. 05.619.21.0016, project ID RFMEFI61919X0016). VNB gratefully acknowledge assistance from a National Science Foundation (NSF) Research at Undergraduate Institutions (RUI) grant no. AST-1909297. GK acknowledges support from NSF grant nos DMS-1363239 and DMS-1900816. Findings and conclusions do not necessarily represent views of the NSF. AM, SD, and AG thank the grant of Russian Science Foundation project 17-12-01335 'Ionized gas in galaxy discs and beyond the optical radius' that supported the spectrophotometric study of gaseous clouds.

Funding for the creation and distribution of the SDSS Archive has been provided by the Alfred P. Sloan Foundation, the Participating Institutions, the National Aeronautics and Space Administration, the National Science Foundation, the U.S. Department of Energy, the Japanese Monbukagakusho, and the Max Planck Society. The SDSS website is http://www.sdss.org/. The SDSS is managed by the Astrophysical Research Consortium (ARC) for the Participating Institutions. The Participating Institutions are The University of Chicago, Fermilab, the Institute for Advanced Study, the Japan Participation Group, The Johns Hopkins University, Los Alamos National Laboratory, the Max-Planck-Institute for Astronomy (MPIA), the Max-Planck-Institute for Astrophysics (MPA), New Mexico State University, Princeton University, the United States Naval Observatory, and the University of Washington.

This research has made use of the NASA/IPAC Extragalactic Database (NED), which is operated by the Jet Propulsion Laboratory, Caltech, under contract with the National Aeronautics and Space Administration. IRAF is distributed by the National Optical Astronomy Observatory, which is operated by the Association of Universities for Research in Astronomy (AURA) under a cooperative agreement with the National Science Foundation. The authors are honoured to be permitted to conduct astronomical research on Iolkam Du'ag (Kitt Peak), a mountain with particular significance to the Tohono O'odham Nation. We thank Tim Heckman for a digital copy of his spectrum of the nucleus of Mkn 1.

REFERENCES

Afanasiev V. L., Moiseev A. V., 2005, Astron. Lett., 31, 194

Baldwin J. A., Phillips M. M., Terlevich R., 1981, PASP, 93, 5

Balick B., Heckman T., 1979, AJ, 84, 302

Crisp R. D., 2009, Bodegom E., Nguyen V., Proc. SPIE 7249, Sensors, Cameras, and Systems for Industrial/Scientific Applications X. SPIE, Bellingham, p. 72490L

Dahari O., De Robertis M. M., 1988, ApJS, 67, 249

Darg D. W. et al., 2010, MNRAS, 401, 1043

de Grijp M. H. K., Keel W. C., Miley G. K., Goudfrooij P., Lub J., 1992, A&AS 96 389

Dodonov S. N., Kotov S. S., Movsesyan T. A., Gevorkyan M., 2017, Astrophys. Bull., 72, 473

Elvis M. et al., 1994, ApJS, 95, 1

Fischer T. C., Crenshaw D. M., Kraemer S. B., Schmitt H. R., 2013, ApJS, 209, 1

Fukugita M., Shimasaku K., Ichikawa T., 1995, PASP, 107, 945

Fullmer L., Lonsdale C. J., 1989, Catalogued Galaxies and Quasars Observed in the IRAS Survey, Version 2, Jet Propulsion Laboratory (JPL D-1932) Ghigo F. D., Wyckoff S., Wardle J. F. C., Cohen N. L., 1982, AJ, 87, 1438

Greene J., Lim J., Ho P. T. P., 2004, ApJS, 153, 93

Groves B. A., Heckman T. M., Kauffmann G., 2006, MNRAS, 371, 1559

Gu Q., Melnick J., Cid Fernandes R., Kunth D., Terlevich E., Terlevich R., 2006, MNRAS, 366, 480

Heckman T. M., Kauffmann G., Brinchmann J., Charlot S., Tremonti C., White S. D. M., 2004, ApJ, 613, 109

Ho L. C., Filippenko A. V., Sargent W. L. W., 1997, ApJS, 112, 315

Józsa G. I. G. et al., 2009, A&A, 500, L33

Kauffmann G. et al., 2003, MNRAS, 346, 1055

Kay L. E., 1994, ApJ, 430, 196

Keel W. C., 1985a, AJ, 90, 577

Keel W. C., 1985b, AJ, 90, 2207

Keel W. C., Kennicutt R. C., Hummel E., van der Hulst J. M., 1985, AJ, 90, 708

Keel W. C. et al., 2012a, MNRAS, 420, 878

Keel W. C. et al., 2012b, AJ, 144, 66

Keel W. C. et al., 2017a, ApJ, 835, 256

Keel W. C. et al., 2017b, PASP, 129, 015002

Keel W. C. et al., 2019, MNRAS, 483, 4847

Kewley L. J., Dopita M. A., Sutherland R. S., Heisler C. A., Trevena J., 2001, ApJ, 556, 121

Kewley L. J., Groves B., Kauffmann G., Heckman T., 2006, MNRAS, 372, 961

Komossa S., Schulz H., 1997, A&A, 323, 31

Kuo C.-Y., Lim J., Tang Y.-W., Ho P. T. P., 2008, ApJ, 679, 1047

LaMassa S. M. et al., 2015, ApJ, 800, 144

Landolt A. U., 1992, AJ, 104, 340

Lang D., Hogg D. W., Mierle K., Blanton M., Roweis S., 2010, AJ, 139, 1782

Lawrence A., Elvis M., 2010, ApJ, 714, 561

Lintott C. J. et al., 2008, MNRAS, 389, 1179

Lintott C. J. et al., 2009, MNRAS, 399, 129

Miller J.S., Stone R.P.S., 1992, Technical Report 66, Lick Obs., Santa Cruz, CA

Mulchaey J. S., Wilson A. S., Tsvetanov Z., 1996, ApJS, 102, 309

Netzer H., 2009, MNRAS, 399, 1907

Omar A., Dwarakanath K. S., Rupen M., Anantharamaiah K. R., 2002, A&A, 394, 405

Phillips M. M., Charles P. A., Baldwin J. A., 1983, ApJ, 266, 485

Pjanka P., Greene J. E., Seth A. C., Braatz J. A., Henkel C., Lo F. K. Y., Läsker R., 2017, AJ, 844, 165

Robitaille T. P., Rossa J., Bomans D. J., van der Marel R. P., 2007, A&A, 464, 541

Ruan J. J. et al., 2016, ApJ, 826, 188

Runnoe J. C. et al., 2016, MNRAS, 455, 1691

Ryan-Weber E. V. et al., 2004, AJ, 127, 1431

Sartori L. F. et al., 2016, MNRAS, 457, 3629

Schawinski K. et al., 2010, ApJ, 724, L30

Schawinski K., Koss M., Berney S., Sartori L. F., 2015, MNRAS, 451, 2517

Schirmer M., Diaz R., Holhjem K., Levenson N. A., Winge C., 2013, AJ, 763, 60

Schweizer F., Seitzer P., Kelson D. D., Villanueva E. V., Walth G. L., 2013, AJ, 773, 148

Shaw R. A., Dufour R. J., 1995, PASP, 107, 896

Stockton A., Fu H., Canalizo G., 2006, NewARv, 50, 694

Stoklasová I., Ferruit P., Emsellem E., Jungwiert B., Pécontal E., Sánchez S. F., 2009, A&A, 500, 1287

Tayal S. S., Zatsarinny O., 2017, ApJ, 850, 147

Thomas D. et al., 2013, MNRAS, 431, 1383

Tody D., 1986, Proc. SPIE, 627, 733

Veilleux S., Goodrich R. W., Hill G. J., 1997, ApJ, 477, 631

Véron-Cetty M.-P., Véron P., 2006, A&A, 455, 773

Wang J., Wei J. Y., He X. T., 2006, ApJ, 638, 106

Werk J. K. et al., 2010, AJ, 139, 279

Whittle M., 1992, ApJS, 79, 49 Wilson A. S., 1996, Vistas Astron., 40, 63

APPENDIX A: PROBABILITY OF AN ARC INTERSECTING A DOUBLE CAP

Given a (double) cone of opening angle $A \le \pi/2$ intersecting the unit sphere $x^2 + y^2 + z^2 = 1$ at two caps, we wish to find the probability P(A, L) that a random geodesic arc of length $L \le 2\pi$ intersects one or both of the caps. In spherical coordinates, the caps are the regions $0 \le \phi \le A$ and $\pi - A \le \phi \le \pi$. Here, we use spherical coordinates θ , ϕ so that $0 \le \theta \le 2\pi$, $0 \le \phi \le \pi$ and $x = \cos \theta \sin \phi$, $y = \sin \theta \sin \phi$, $z = \cos \phi$.

We shall compute the probability using conditional probabilities. Let C denote the centre of the random geodesic arc and $\theta(C)$, $\phi(C)$ the corresponding spherical coordinates. Let $P(A, L, \phi)$ denote the probability that the arc intersects a cap given that $\phi(C) = \phi$. Then,

$$P(A, L) = \int_0^{\pi} P(A, L, \phi) \frac{1}{2} \sin \phi d\phi,$$

= $2 \int_0^{\pi/2} P(A, L, \phi) \frac{1}{2} \sin \phi d\phi,$ (A1)

where $\frac{1}{2}\sin\phi\mathrm{d}\phi$ is just the probability density for $\phi(C)$. Namely, the probability that $a<\phi(C)< b$ is obtained by integrating $\frac{1}{4\pi}\int_a^b\int_0^{2\pi}\sin\phi\mathrm{d}\theta\mathrm{d}\phi=\int_a^b\frac{1}{2}\sin\phi\mathrm{d}\phi$ which is the proportion of the sphere in the range $a<\phi< b$.

The expression on the right in equation (A1) reflects the symmetry that the probabilities are the same for ϕ and $\pi - \phi$. So, we only need to consider $0 \le \phi \le \pi/2$.

Some simple cases are recorded below

$$P(A, L, \phi) = \begin{cases} 0 & \text{if } A + L/2 \le \phi \le \pi/2, \\ 1 & \text{if } 0 \le \phi \le A. \end{cases}$$

The first case corresponds to values of ϕ where the arc cannot reach a cap no matter which way it points, the second case corresponds to when the centre of the arc lands in a cap. We now discuss a third case, when $A < \phi < \min \{\pi/2, A + L/2\}$.

To begin, there is no harm in assuming $\theta(C) = 0$ since the problem is rotationally symmetric. Then, $C = (\sin \phi, 0, \cos \phi)$. The vec-

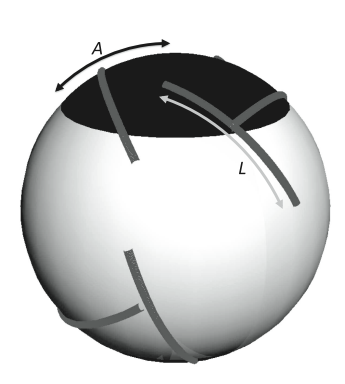


Figure A1. Illustration of quantities used in the bicone-arc intercept calculation. As projected on a unit sphere, the black shading shows the cap spanned by one half of the notional ionization (bi)cone, with opening angle A. The dark grey arcs are randomly oriented with angular length L, representing in our study the extent of H I outside the host galaxy as seen by the nucleus. We aim to determine the typical value of A based on using ionized gas to trace the number of intercepts of arcs of various measured angular extent, based on the assumption that ionized gas will be detected at locations of such intercepts.

tors $\mathbf{a} = \langle \cos \phi, 0, -\sin \phi \rangle$, $\mathbf{b} = \langle 0, 1, 0 \rangle$, $\mathbf{c} = \langle \sin \phi, 0, \cos \phi \rangle$ are pairwise perpendicular and can be used to form a local coordinate system at C (they are a rotated version of i, j, k). The arc centered at C can be parametrized via

 $c(t) = (\sin t \cos \theta)a + (\sin t \sin \theta)b + (\cos t)c.$

This is derived by treating a, b, c as we would usually treat i, j, k in spherical coordinates. Here, $-L/2 \le t \le L/2$ and θ will now be used to represent the angle the arc makes with a. By symmetry we may assume $0 \le \theta \le \pi/2$.

It helps to recall the inequality

$$|a\sin t + b\cos t| \le \sqrt{a^2 + b^2}. (A2)$$

Equality occurs exactly when

$$(\sin t, \cos t) = \frac{\pm 1}{\sqrt{a^2 + b^2}}(a, b).$$
 (A3)

The great circle containing our geodesic arc intersects a cap if there is a value of t such that the z-coordinate of c(t) is $\pm \cos A$; i.e.

$$\pm \cos A = -\sin t \cos \theta \sin \phi + \cos t \cos \phi. \tag{A4}$$

Setting $a = -\cos\theta \sin\phi$ and $b = \cos\phi$ in equation (A2), equation (A4) has a solution exactly when $\cos^2 A \le \cos^2\theta \sin^2\phi + \cos^2\phi = 1 - \sin^2\theta \sin^2\phi$. This is equivalent to $\sin\phi \sin\theta \le \sin A$, and the maximal possible angle θ such that the great circle intersects a cap is $\theta_{\text{max}} = \sin^{-1}(\frac{\sin A}{\sin\phi})$. The corresponding values of t satisfy

$$(\sin t, \cos t) = \frac{\pm 1}{\cos A} (-\cos(\theta_{\text{max}})\sin\phi, \cos\phi) \text{ by (A3)}.$$
 (A5)

Since A, ϕ , θ_{max} are all in the range $[0, \pi/2]$, $\sin t$ and $\cos t$ have opposite signs that means $(\sin t, \cos t)$ is in quadrants IV and II. Therefore, the closest point of intersection occurs when $-\pi/2 \le t \le 0$ and this means the great circle intersects both caps or no caps. In particular, if $L/2 \ge \pi/2$, then the arc intersects the cap for θ in the range $0 \le \theta \le \sin^{-1}(\frac{\sin A}{\sin \phi})$.

This shows that for $L > \pi$

$$P(A,L) = 2\left(\frac{1}{\pi}\int_A^{\pi/2}\sin^{-1}\left(\frac{\sin A}{\sin\phi}\right)\sin\phi\mathrm{d}\phi + \int_0^A\frac{1}{2}\sin\phi\mathrm{d}\phi\right),$$

which does not depend on L.

For $L < \pi$, the arc intersects the cap in the full sweep $0 \le \theta \le \theta_{\max}$ as long as the intersection point at the maximal angle occurs for $|t| \le L/2$, or equivalently $\cos t \ge \cos L/2$. By equation (A5), $\cos t = \frac{\cos \phi}{\cos A}$ at the maximal angle, and when $\cos L/2 \le \frac{\cos \phi}{\cos A} = \cos t$ the arc intersects the cap for $0 \le \theta \le \sin^{-1} \frac{\sin A}{\sin \phi}$. Namely, for each ϕ with A

$$\leq \phi \leq \cos^{-1}(\cos A \cos(L/2))$$
, we get $P(A, L, \phi) = \frac{2}{\pi} \sin^{-1} \left(\frac{\sin A}{\sin \phi}\right)$.

If the arc does not intersect the cap in the full range $0 \le \theta \le \theta_{\text{max}}$, then $\phi > \cos^{-1}[\cos A\cos(L/2)]$. Assuming also $A + L/2 \ge \phi$, so that the arc can actually intersect the cap, the maximal angle at which the arc intersects the top cap occurs when t = -L/2. From equation (A4), when t = -L/2

$$\cos\theta = \frac{\cos A - \cos(L/2)\cos\phi}{\sin(L/2)\sin\phi},$$

making the range of θ given by $0 \le \theta \le \cos^{-1}(\frac{\cos A - \cos(L/2)\cos\phi}{\sin(L/2)\sin\phi})$. So, $P(A,L,\phi) = \frac{2}{\pi}\cos^{-1}(\frac{\cos A - \cos(L/2)\cos\phi}{\sin(L/2)\sin\phi}) \quad \text{for } \cos^{-1}(\cos A\cos(L/2)) < \phi \le \min\{\pi/2,A+L/2\}.$

We can now compute P(A, L) according to two cases: For $L > \pi$

$$P(A, L) = \frac{2}{\pi} \int_{A}^{\pi/2} \sin^{-1} \left(\frac{\sin A}{\sin \phi} \right) \sin \phi \, d\phi + 1 - \cos A.$$

For $L < \pi$

$$\begin{split} P(A,L) &= 1 - \cos A + \frac{2}{\pi} \int_A^{\cos^{-1}(\cos L/2\cos A)} \\ &\times \sin^{-1}\left(\frac{\sin A}{\sin \phi}\right) \sin \phi \; \mathrm{d}\phi \\ &+ \frac{2}{\pi} \int_{\cos^{-1}(\cos(L/2)\cos A)}^{\min\{\pi/2,A+L/2\}} \\ &\times \cos^{-1}\left(\frac{\cos A - \cos(L/2)\cos \phi}{\sin(L/2)\sin \phi}\right) \sin \phi \; \mathrm{d}\phi. \end{split}$$

APPENDIX B: POTENTIAL EMISSION-LINE CANDIDATES

Our narrow-band images show some potential compact emission-line sources in the fields of the target galaxies, many in the range of size and luminosity (at the target galaxy redshift) associated with emission-line dots (ELdots), similar to those seen as outlying star-forming regions by Ryan-Weber et al. (2004) and Werk et al. (2010). They are listed in Table B1, with an indication of whether they are projected inside, near the edge of, or outside the lowest-density H1 contours shown by Kuo et al. (2008) and Greene et al. (2004). The locations of these emission candidates are shown in Fig. B1.

Of the whole set, three are projected within the H I detection regions, and four lie close to those contours (within about 15 per cent in radius). The emission-line candidates' locations are given both by coordinates and by projected radius and position angle from the targeted galaxy nucleus. We designate candidates by letters for each field where there is more than one. Detection limits for emission-line point sources are typically $5 \times 10^{-16} \, \mathrm{erg \, cm^{-2} \, s^{-1}}$. These fluxes were measured via the IRAF task *imexamine*, with fitting radius fixed at 5 arcsec and sky annulus centred at four times the image FWHM. Since the difference images used to seek [O III] emission were scaled for the colours of the outer parts of the host galaxies, there will be flux errors depending on colour.

We examined these positions in SDSS DR7 and DR14 data, which provided additional information on some of the candidates. A few appear in SDSS DR7 but not later data releases, appearing close to bright stars whose exclusion zones are larger in the later processing versions. These 'vanishing' SDSS objects are the one in the field of Mkn 1, and Mkn 341 E and F, which are compact emission knots in a pair of interacting galaxies whose photometric redshifts z = 0.050, 0.096 suggest that the detected emission is H β . NGC 513 B is a background QSO at z = 2.215, where the emission we detect is part of the broad C IV $\lambda 1549$ profile. We omit objects whose fluxes are compromised by adjacent bright star images, as probably not being genuine emission sources. Objects matching SDSS, 2MASS, or XMM sources are listed by those coordinate designations; coordinates without such an identifier are measured from our data (particularly for the fields of Akn 539, UGC 3157, and MS 04595+0327, which were not covered by SDSS imagery).

Table B1. Compact emission-line candidates.

Field-ID	(Possible) name or coordinates	HI Loc.	r_{proj} (arcsec)	r_{proj} (kpc)	P.A. (°)	F(5007) (erg cm ⁻² s ⁻¹)	Notes
Akn 539 A	18:29:01.58 +50:23:50.2	Outside	151	52	54.8	4.0×10^{-15}	
Akn 539 B	18:29:07.51 +50:20:35.4	Inside	216	74	121	4.2×10^{-15}	
Akn 539 C	18:29:07.89 +50:21:33.9	Inside	194	66	102	3.8×10^{-15}	
Akn 539 D	18:28:57.85 +50:25:37.8	Outside	223	76	25.3	3.5×10^{-15}	
Mkn 1	2XMM J011601.3+330821	Outside	204	65.	345	4.1×10^{-14}	
Mkn 341 A	2MASX J00364502+2405313	Outside	389	120	317	6.4×10^{-15}	
Mkn 341 C	SDSS J003632.35+240229.4	Outside	334	103	307	5.2×10^{-15}	
Mkn 341 D	2MASX J00365081+2355293	Outside	212	65	185	1.2×10^{-14}	
Mkn 341 E	SDSS J003706.15+235529.8	Outside	282	87	138	1.1×10^{-14}	
Mkn 341 F	SDSS J003706.42+235450.5	Outside	318	98	142	1.1×10^{-14}	Knot in interacting
							pair
Mkn 461 A	13:47:20.0 +34:10:52	Edge	104	24	14.5	1.3×10^{-14}	
Mkn 461 B	13:47:23.0 +34:11:16	Edge	186	44	21.0	1.3×10^{-14}	
MS 04595+0327 A	05:02:16.6 +3:33:46.7	Outside	160	52	46.0	1.1×10^{-13}	
MS 04595+0327 B	05:02:01.8 + 3:29:15.1	Outside	187	60	213	1.2×10^{-13}	
NGC 513 A	2XMM J012434.2+334732	Outside	105	41	134	3.3×10^{-15}	
NGC 513 B	2XMM J012437.0+335004	Outside	134	53	41	3.2×10^{-15}	QSO, $z = 2.215$
NGC 5548 A	SDSS J141742.11+250411.4	Outside	344	119	227	1.6×10^{-15}	
NGC 5548 B	SDSS J141743.50+250400.1	Outside	320	111	220	1.4×10^{-15}	
NGC 5548 C	SDSS J141745.92+250838.6	Outside	173	60	275	1.5×10^{-15}	
NGC 5548 D	2XMM J141746.9+250725	Outside	172	60	257	1.2×10^{-15}	
NGC 5548 E	SDSS J141801.79+251108.3	Outside	160	56	7.0	8.6×10^{-16}	
NGC 5548 F	SDSS J141802.14+251030.4	Outside	135	47	12.0	1.1×10^{-15}	
NGC 5548 G	SDSS J141805.94+250416.3	Edge	258	90	155	1.1×10^{-15}	
NGC 5548 H	SDSS J141818.19+250612.6	Edge	281	98	114	5.0×10^{-16}	
UGC 3157 A	04:46:29.9 +18:24:43	Outside	179	56	246	1.4×10^{-14}	
UGC 3157 B	04:46:28.4 +18:27:42	Inside	19.7	86	278	1.6×10^{-14}	Knot in spiral arms of UGC 3157
UGC 3995	SDSS J074409.03+291228.5	Outside	320	102	165	2.3×10^{-14}	

Note. H I Loc denotes whether the emission-line candidate is within, near the edge, or outside of the H I emission detected by Kuo et al. (2008). Each candidate is at a projected radius r_{proj} , in arcsec and kpc, from the targeted AGN host galaxy. This location is at position angle given by PA, in degrees north through east, from the AGN host. We measure a flux in the emission line listed as F(5007).

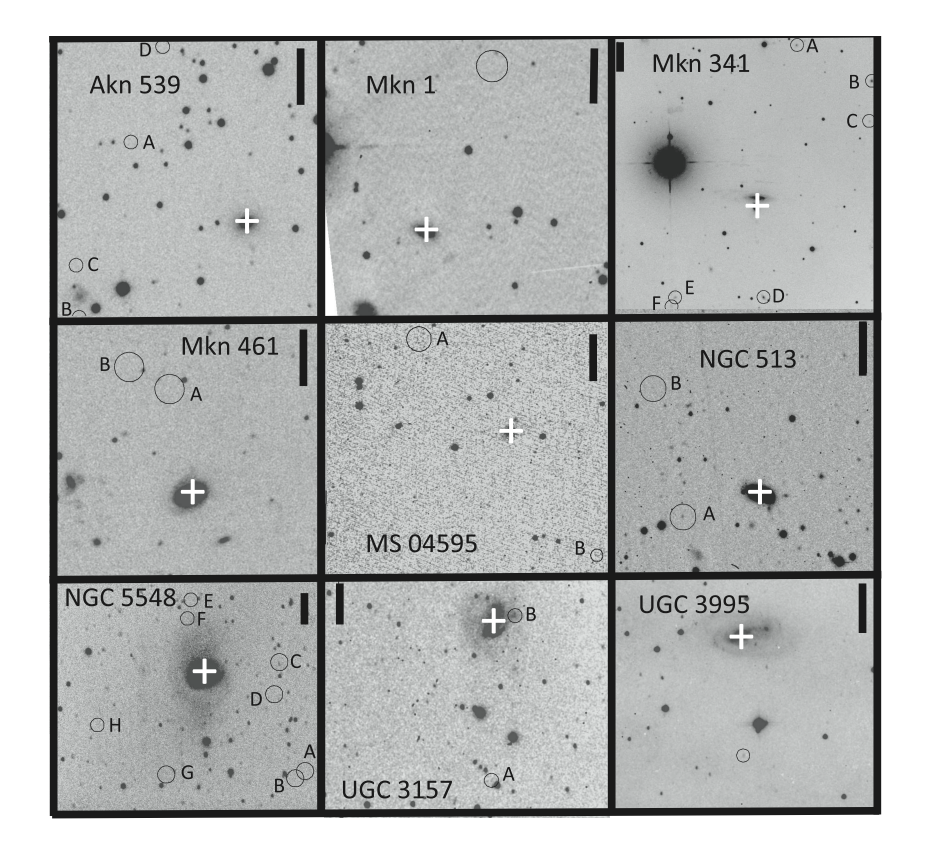


Figure B1. Locations of additional candidate emission-line objects in the fields of surveyed AGN. Each AGN is marked with a white cross, and emission candidates are circled. North is at the top and east to the left; to show details in the fields and include the detected objects, the scale varies between fields and is indicated by the vertical scale bars, each spanning one arcminute. The underlying images are through our 510-nm filter.

This paper has been typeset from a TEX/IATEX file prepared by the author.